Cyclic oxidation of alloy 718 produced by additive manufacturing compared to a wrought-718 alloy

Tom Sanviemvongsak, Daniel Monceau, Martin Madelain, Clara Desgranges, James Smialek, Bruno Macquaire

Version of Record: https://www.sciencedirect.com/science/article/pii/S0010938X21005709
Manuscript_816d0d6342dbd4d14d1e67353d915fe3

Cyclic oxidation of alloy 718 produced by additive manufacturing compared to a wrought-718 alloy

Tom Sanviemvongsak [a,b*], Daniel Monceau [a], Martin Madelain [a], Clara Desgranges [b], James Smialek [c], Bruno Macquaire [b]

[a] CIRIMAT, Université de Toulouse, CNRS, INPT, ENSIACET, 4 allée Emile Monso, BP 44362, 31030 Toulouse Cedex 4, France
[b] Safran Tech, Rue des Jeunes Bois, Châteaufort, CS 80112, 78772 Magny-Les-Hameaux, France
[c] Retired from NASA Glenn Research Center, Cleveland, OH 44135, USA

*Corresponding author contact information:
Address : CIRIMAT, Université de Toulouse, CNRS, Toulouse INP, ENSIACET, 4 allée Emile Monso, BP 44362, 31 030 Toulouse Cedex 4, France;
E-mail address: tom.sanviemvongsak@ensiacet.fr

Abstract

The cyclic oxidation resistance at 900 °C of the alloy 718 produced by laser beam melting and electron beam melting was compared to that of the wrought-718 alloy. Results showed large differences regarding the rate of oxide layer spallation. The wrought alloy presents much more adherent oxide scale. Moreover, the standard heat treatment and the surface grinding slightly delay the catastrophic spallation. The role of sulfur and manganese on the adhesion of the oxide scale is quantitatively discussed using thermodynamic modelling. This result may force restrictions on the chemical composition of the alloy 718 powder used for additive manufacturing.

1. Introduction

The high temperature oxidation resistance of Ni-base alloys produced by Additive Manufacturing (AM) is a new and active topic, and several publications can be found in the opened literature since 2014. The alloy 718 is the one the most popular nickel base superalloys produced by additive manufacturing and one of the most studied in the oxidation field. Although the initial microstructures of AM-718 alloys are different from cast or wrought alloys, available experimental results do not show much difference regarding their high temperature isothermal oxidation resistance [1-3]. However, when these alloys produced by AM have a poor metallurgical state - a low density with the presence of cracks or pores - they present much higher oxidation kinetics than a wrought alloy [4]. Optimized AM process parameters are now available to produce dense 718 alloys. Heat treatments are used to release

most of the internal stress and to get closer to the microstructure of a conventional-718 alloy (wrought or cast). The literature results regarding the effect of heat-treatments on the oxidation resistance are not unanimous. Some researchers showed that standard heat treatments carried out on the alloy 718 produced by AM do not have significant effect on its high temperature oxidation resistance [2, 5, 6]. Conversely, Sadeghi *et al.* showed that the conventional heat treatment (AMS5662) and a high isostatic pressure (HIP) treatment increase the oxidation resistance at 850 °C of the alloy 718 produced by electron beam melting (EBM) [7]. This result was mainly attributed to densification and the homogenization of the microstructure compared to the as-built sample.

In aircraft turbines, alloy 718 components are exposed to thermal cycles (take-off, cruising, landing) which induce thermal strains of the oxide layer and its metallic substrate. These deformations generate stresses that can be relaxed by plastic deformation of the oxide layer and/or the metal, by cracking of the oxide layer (shear stress), by decohesion of the oxide layer [8], or by creep of the metal and the fine grained oxide scale [9]. Laboratory cyclic air oxidation tests are carried out to simulate these operating cycles in a simplified manner. They allow to evaluate the growth kinetics of the oxide layers and their adherence to the alloy. Up to now, only one publication reports cyclic oxidation behaviour of the alloy 718 produced by AM. The Oak Ridge laboratory showed that EBM-718 alloys present lower mass losses than a wrought-718 alloy, when they were exposed to cyclic humid air oxidation at 750 °C [10]. This result was attributed to the formation of iron oxides on the surface of the AM samples, which would result in a greater mass gain for the EBM samples. However, this result remains unquantified and it is not clear whether the mass gain due to iron oxide formation is greater than the mass loss due to spalling. More recently, in the same research group, Romedenne *et al.* studied the cyclic oxidation in air at 950 °C of Hastelloy X alloy produced by LBM and EBM, comparing their behaviour to that of the wrought alloy [11]. They found out that the oxide scale of the Hastelloy X alloy produced by EBM and LBM spalled faster than the wrought alloy. This result was mainly attributed to the precipitation of a thin layer of SiO_2 at the metal/Cr_2O_3 interface.

One of the main characteristics of AM parts is their high roughness when compared to machined ones. High roughness has some specific effects such as enhanced isothermal oxidation kinetics in terms of mass gain due to a higher reactive surface area [1, 12], or accelerated protective element depletion (Cr depletion here) in convex areas [13]. As AM technology users would like to use as-built parts, it is important to study as-built samples.

Nevertheless, it is also important to study ground or polished samples to dissociate the effects of chemistry, microstructure and surface geometry.

In the present paper, the cyclic air oxidation resistance of the alloy 718 produced by LBM and EBM process is compared to that of a commercial heat-treated wrought alloy (AMS5662). The effect of the surface roughness, the heat treatment and the chemical compositions on the oxide scale adhesion will be discussed.

2. Materials and experimental procedures

The alloy 718 samples were produced using laser beam melting (LBM, EOS M290) and electron beam melting (EBM, Arcam A2X). They were produced at Safran (Safran Additive Manufacturing, Magny-les-Hameaux, France) with the machine manufacturer's standard settings, respectively EOS^{TM} and ARCAM^{TM}. The alloys were studied in their as-built form and compared to those heat-treated. The heat-treatment of LBM samples consisted of a homogenization treatment under vacuum at 1095 °C for 1 h, followed by natural cooling in the cold section of the furnace until they reached room temperature. The p_{O_2} was estimated to be below 0.01 mbar during this heat treatment. Then followed a precipitation hardening treatment at 760 °C during 5 h under vacuum, followed by 1 °C/min cooling rate in order to reach 650 °C and held 1 h, then finally cooled in the chamber until they reached room temperature. The AM samples were compared to the heat-treated wrought (WRG) alloy 718 (AMS 5662) provided by Aubert et Duval (Ancize, France), their 718 ingots were hot rolled. A more detailed description of these alloys can be found in a previous paper [1], which contains the characterization of their chemical composition, microstructure and the description of the AM parameters used to build these samples. Their dimensions approached 15 × 10 × 2 mm. Some samples surfaces were ground using P600-SiC paper and others were studied with their raw surfaces. To remove the initial roughness, the grinding needed to remove less than 150 ± 40 μm from the raw LBM sample and less than 600 ± 60 μm deep from the raw EBM sample. After grinding, samples were ultrasonically cleaned in acetone and ethanol, then dried.

The initial chemical compositions of the three alloys were quantified using an electron probe microanalyser (EPMA, SX Five FE CAMECA) calibrated on standards at 7 kV and 20 nA. Moreover, the concentration of minor and impurity elements (Y, La, Ce, Re, Co, Si, B, P, S, Ta and Mn) were measured using glow discharge mass spectrometry (GDMS, Astrum Nu

Ametek®). This measurement has 20 % relative uncertainty regardless of the nature of the analysed element and its quantity. The concentration of carbon was measured with instrumental gas analyser (IGA, Horiba EMIA 820V) with a measurement uncertainty of around 2% (for 500 ppm wt. of C). The grain size evaluations were performed using a scanning electron microscope (JEOL JSM-7100TTLS LV) equipped with an EBSD camera (NordlysNano, Oxford Instruments).

The cyclic air oxidation tests were conducted in a vertical cyclic oxidation rig at the CIRIMAT laboratory (Toulouse, France). The samples were hanged with FeCrAlY hooks on FeCrAl ODS plates. Hooks were preoxidised 1 h at 1100 °C in order to form a very adherent and slow growing alumina scale. The temperature was set using a type-K thermocouple welded to a spare 718 sample. The monitoring of the temperature was assured by a type-S thermocouple located near the samples. Samples underwent cycles with 1 h hot dwell at 900 °C in low velocity laboratory air (vertical partially opened tube) and 15 min of cooling under pulsed lab air flow. The temperature of all the samples reached the room temperature in less than 10 min. All samples were weighed with the Sartorius ME215P balance with ± 20 µg accuracy.

3. Results and discussions

3.1. Oxidation kinetics

The cyclic oxidation tests were conducted at 900 °C under laboratory air. They were performed to evaluate the effect of manufacturing processes, surface roughness and heat treatment on the oxidation resistance of the alloy 718 produced by LBM, EBM and wrought process. Results are shown in **Figure 1**. In contrast to the isothermal and cyclic oxidation tests conducted at 850 °C in a previous paper [1, 14] the cyclic oxidation tests at 900 °C show large differences between these three 718 alloys in terms of mass variation ($\Delta m/s$). As seen in **Figure 1(a)**, the LBM samples, whether ground or raw, treated or untreated, show the worst resistance to cyclic oxidation compared to the as-built EBM sample and the heat-treated wrought specimen. As shown in **Figure 1(b)**, the LBM samples with raw surfaces present the highest mass gain; this result is due to a higher surface area as shown previously through a quantitative evaluation [1]. The spallation rate of the oxide layer on LBM samples is very fast after 600 to 900 cycles, compared to 1600 cycles for the EBM sample. On the other hand, the oxide scale on the wrought sample spalled but slower than the AM samples. The low negative slope of the oxidation kinetics of the wrought sample shows that its oxide scale is more

adherent than that of the AM samples. The mass gain of all samples, reached a maximum value between 0.7 and 1.0 mg.cm^{-2} before the spallation of the oxide layer becomes predominant. This kind of mass gain corresponds to a thickness of the oxide scale less than 5 µm. The results on the LBM specimens show weak but consistent effects of ground surfaces and heat treatments. These two parameters postpone the accelerated spallation of the LBM samples by about 100 cycles and even 400 cycles when the samples were ground and heat-treated.

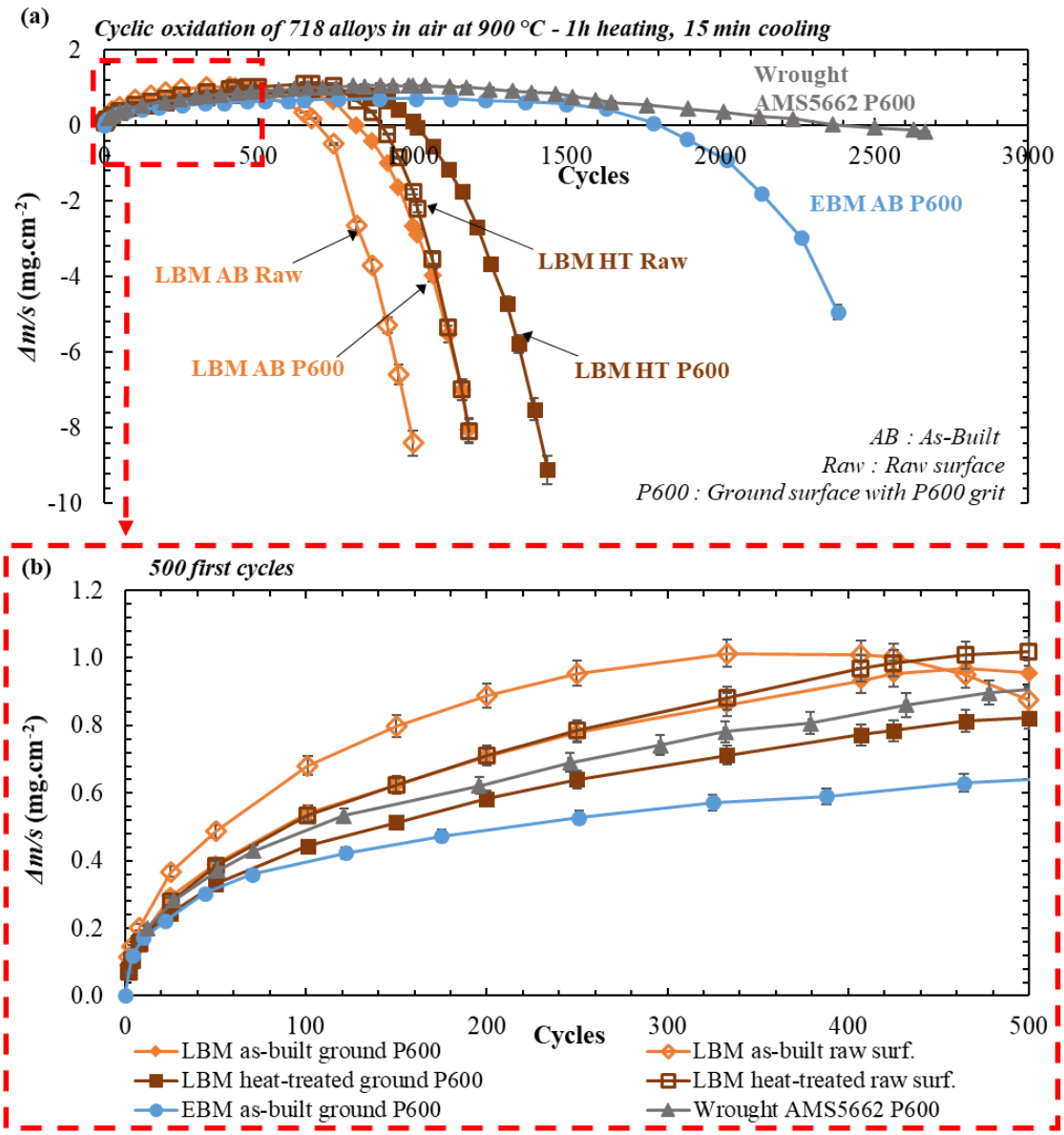

Figure 1. Cyclic oxidation kinetics in laboratory air at 900 °C of 718 alloys produced by LBM, EBM and wrought processes (cycles of 1 h at 900 °C and 15 min cooling down to room temperature).

Cyclic oxidation kinetics were quantified using the "p-k_p" kinetic model in its Monte Carlo version. This numerical model, initially elaborated in 1998 [15] was used in several works (e.g. [16]) and was reprogrammed in Python language for this study [17]. This model is similar to the random spall site model version of NASA's COSP [18]. In this model, the surface is divided in hundreds or thousands of cells. In this version, the oxide growth and spallation on a particular cell do not depend on the neighboring cells. At each time step, corresponding to the duration of a high temperature dwell, the oxide scale growth is calculated as a function of the current oxide scale thickness and of the parabolic constant k_p. Then, the oxide scale spalls with a probability p during cooling or heating. In this version of the model, p and k_p do not depend on the local oxide thickness, but they depend on time. Indeed, the pairs of p-k_p values were determined for all oxidised samples by adjusting the model parameters in order to reproduce the experimental curves of mass variation. All curves were fitted using three successive pairs of p-k_p values as shown in **Figure 2**. These successive pairs represent different oxidation regimes. Results are presented in **Table 1** and these pairs of p-k_p values are compared on the performance map [19, 20], **Figure 3**.

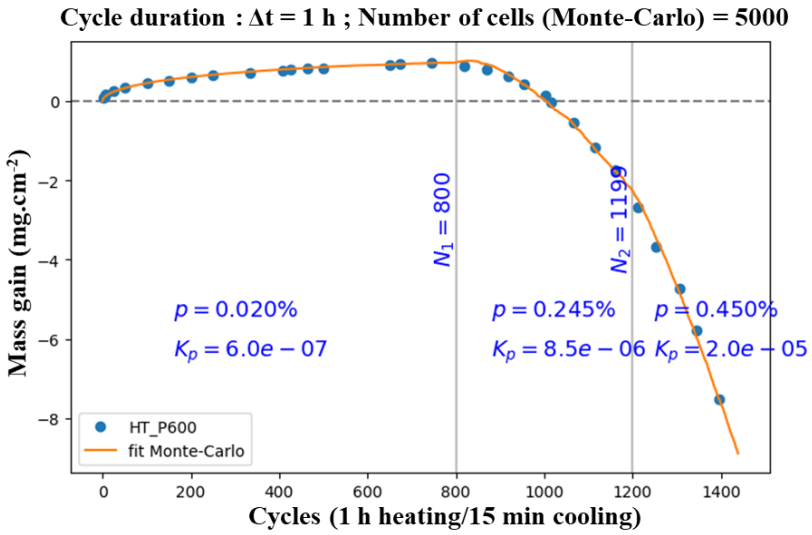

Figure 2. Example of cyclic oxidation adjustment made with "p-k_p" model in its Monte-Carlo version, three successive pairs of "p-k_p"-values were used to fit the cyclic oxidation kinetics of the ground heat-treated LBM-718 sample oxidised in laboratory air at 900 °C.

Table 1. Pairs of p-k_p values determined for cyclic oxidation kinetics oxidised under laboratory air at 900 °C of alloys 718 produced by LBM, EBM and wrought (1 h at 900 °C and 15 min of cooling).

		Nb cycles	k_p ($mg^2.cm^{-4}.s^{-1}$)	p (%)
LBM as-built, raw surf.	1st stage	430	1.6×10^{-6}	0.05
	2nd stage	730	3.0×10^{-6}	0.13
	3rd stage	1002	7.0×10^{-6}	0.7
LBM as-built, P600	1st stage	720	1.3×10^{-6}	0.05
	2nd stage	1000	1.0×10^{-5}	0.3
	3rd stage	1183	2.0×10^{-5}	0.5
LBM, heat-treated, raw surf.	1st stage	750	8.0×10^{-7}	0.02
	2nd stage	930	6.0×10^{-6}	0.3
	3rd stage	1183	2.0×10^{-5}	0.6
LBM heat-treated P600	1st stage	800	6.0×10^{-7}	0.02
	2nd stage	1200	8.5×10^{-6}	0.245
	3rd stage	1438	2.0×10^{-5}	0.45
EBM as-built P600	1st stage	1520	4.0×10^{-7}	0.024
	2nd stage	2100	3.0×10^{-6}	0.115
	3rd stage	2380	5.0×10^{-6}	0.24
Wrought AMS5662	1st stage	1100	6.7×10^{-7}	0.019
	2nd stage	2350	6.2×10^{-7}	0.03
	3rd stage	2664	6.7×10^{-7}	0.022

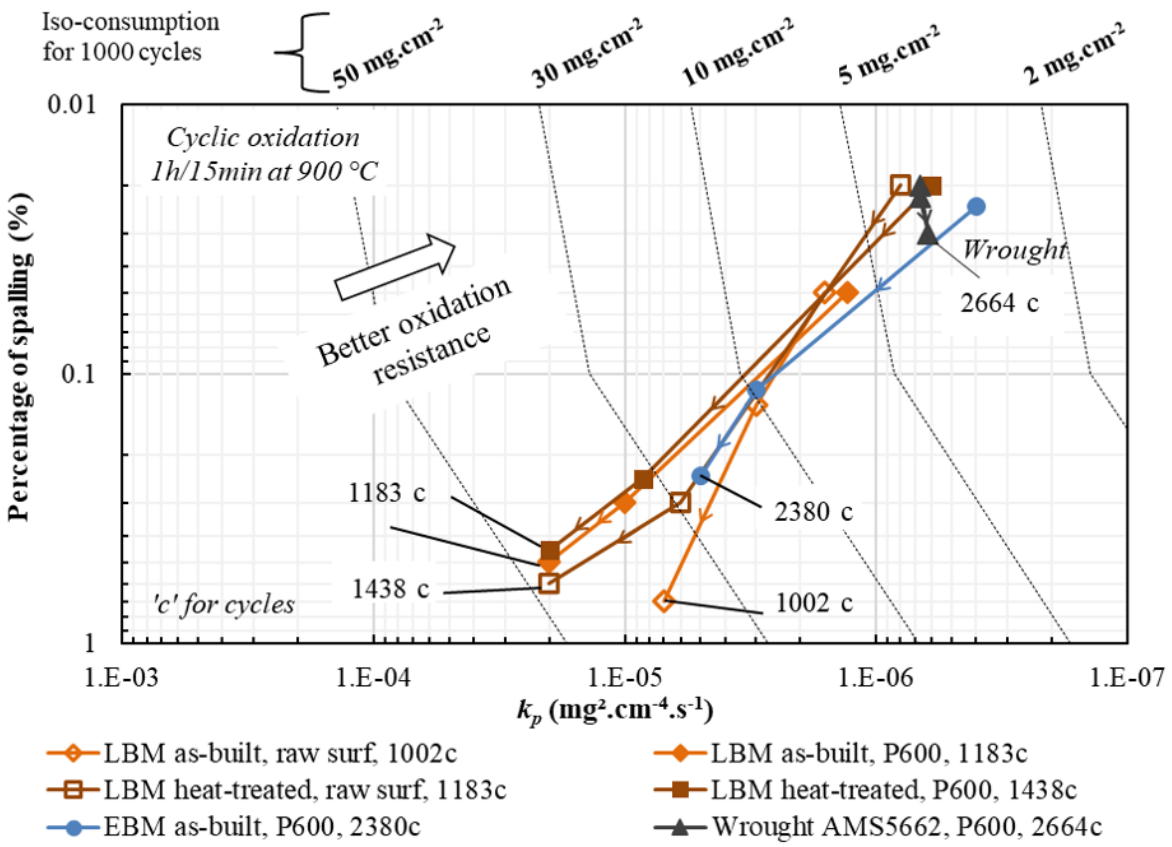

Figure 3. "*p*-k_p" performance map of the alloys 718 produced by LBM, EBM and wrought oxidised under laboratory air at 900 °C (1 h at 900 °C and 15 min cooling).

Results for AM samples show a similar evolution of pairs of *p*-k_p values, whether produced by LBM or EBM processes. The "worst" pairs of *p*-k_p values (highest values) are those obtained on LBM samples. After 1000 cycles, the latter show high k_p values, ranging from 7.0×10^{-6} to 2.0×10^{-5} mg².cm^{-4}.s^{-1}, as well as spalling percentages reaching values between 0.30% and 0.70%. The EBM sample follows the same catastrophic mass loss kinetics as LBM samples but with a delay of nearly 1000 cycles. After 2380 cycles, the cyclic oxidation kinetics of the EBM sample reaches a k_p value of 5.0×10^{-6} mg².cm^{-4}.s^{-1} and a spalling percentage of 0.24%. The wrought sample, on the other hand, has lower *p*-k_p values, even after undergoing 2664 cycles, with k_p reaching 6.7×10^{-7} mg².cm^{-4}.s^{-1} and a spalling percentage of 0.02%, these values are an order of magnitude lower than those determined for LBM and EBM samples. In addition, during the first stage of the cyclic oxidation tests with very little spallation, all values of k_p are found close to each other. They are even lower than those found previously by Al-Hatab *et al.* for heat-treated commercial 718 samples tested under cyclic air oxidation at 750, 850 and 950 °C [21].

It is remarkable to note in **Figure 3**, that all p-k_p values of AM alloys follow the same "path", they certainly degrade in the same way, but not with the same speed. During the reaction, the final metal consumption of AM alloys is 10 times faster than the wrought alloy. The iso-consumption of chromium began at around 4 $mg.cm^{-2}$ and reached 50 $mg.cm^{-2}$ for 1000 cycles, which corresponds approximately to a consumption of metal of 60-µm thick for 1000 cycles. Furthermore, it would take a much longer test time at 900 °C to see if the wrought sample follows the same degradation route as the AM samples.

3.2. Discussions regarding the adhesion of the oxide scale

3.2.1. Effect of the heat-treatment

The cyclic oxidation kinetics at 900 °C presented in **Figure 1** showed that the homogenisation heat-treatment (solution treatment and ageing) delayed the catastrophic scaling of the LBM samples by about 100 cycles. The effect is not excessive, but this result was observed on ground samples and those with rough surfaces. According to literature, the homogenisation heat-treatment applied to the alloy 718 produced by AM, leads to a microstructure close to that of the wrought heat-treated alloy. This treatment removes traces of melting pools and microsegregation areas [22]. Calandri *et al.* [6] showed the benefit of an optimized heat-treatment on the redistribution of Nb in the alloy 718 produced by LBM, but they didn't show its effect on the oxidation resistance. Moreover, McDowell *et al.* showed that an alloy with smaller grains and therefore a higher density of diffusion short-circuit paths has a higher diffusion flux of protective element (Cr) to the surface than an alloy with larger grains [23]. Therefore, alloys with small grains, such as wrought alloys, would form a protective oxide layer quicker and experience lower mass gains. However, EBSD analyses conducted on oxidised samples presented in **Figure 4** and **Table 2**, show that the ground EBM alloy has larger grains than the LBM and wrought alloys, yet it has the lowest mass gain and presents a better cyclic oxidation resistance than the LBM alloy.

In addition, it has been shown previously [1, 24] that even if the AM samples were studied in their as-built forms and compared to the heat-treated wrought sample, the three alloys - EBM, LBM and wrought - had similar oxidation resistances in terms of mass change after 3000 h in air at 850 °C. Their microstructure differences had only a small effect on the morphology of the oxide at the grain boundaries [24]. In the present study, cyclic condition at 900 °C shows that the solution heat-treatment conducted on LBM samples has a small positive effect on the

adhesion of the oxide scale, which may be attributed to the homogenization of the microstructure.

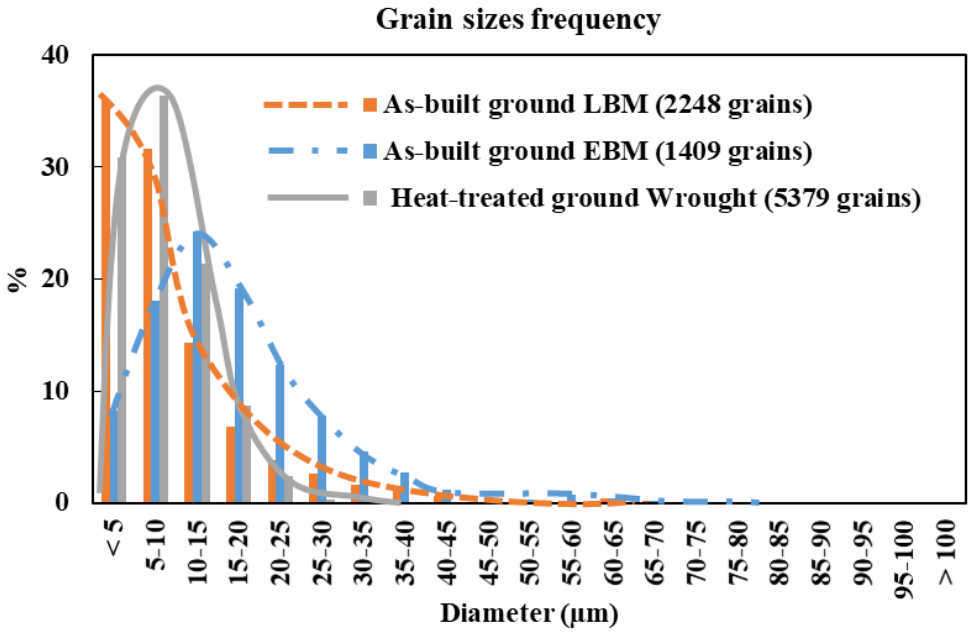

Figure 4. EBSD analyses of grain size distribution of the three alloys after oxidation, observed in the (XY) plan perpendicular to the built direction of AM samples (size of the analysed area under the oxide scale: 1500 × 130 µm²).

Table 2. Average grain sizes of LBM, EBM and wrought alloys, extracted from the EBSD analyses.

	LBM	EBM	Wrought
Nb of grains	2248	1409	5379
Avg. grain sizes	10.3 µm	17.3 µm	9.0 µm
2σ	10.4 µm	11.1 µm	5.3 µm

3.2.2. Effect of surface defects

Surface defects in AM samples may also be a source of catastrophic spallation. Indeed, sintered powder particles or "spatter" type defects were observed on specimens with rough surfaces in **Figure 5(b)** and **(d)**. These surface asperities can be removed more easily, particularly if the interface between the sintered solid particle and the alloy is susceptible to oxidation. It has been shown previously [1] that this interface may exhibit rutile-type titanium oxide (TiO_2). The growth of this oxide at the particle/surface interface can then cause a

greater loss of material. In addition, Evans *et al.* have shown that asperities generated by the surface topography can lead to deformation of the alloy at the metal/oxide interface during thermal cycling, leading to the initiation of fatigue cracking in the oxide layer [25]. Higher surface roughness leads to more areas under compressive stress concentration. However, the oxidation kinetics in **Figure 1**, shows that the oxide scales of the ground LBM specimens are susceptible to spallation as catastrophic as the spallation rate of the oxide scale developed on the rough-surface specimens, but about 100 cycles later.

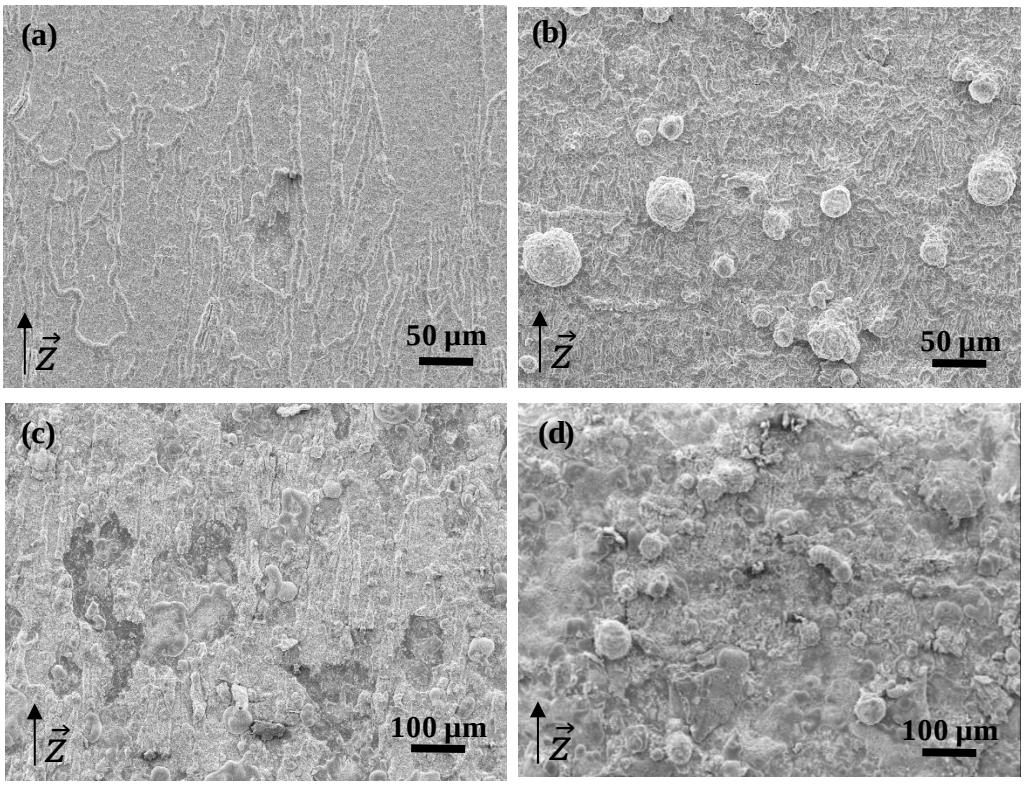

Figure 5. SEM-SE micrographs of the ground (P600) surface LBM specimen on the (XZ) plane after (a) 500 cycles and (c) 1438 cycles, and of the raw surface of LBM specimen after (b) 500 cycles and (d) 1183 cycles, all samples were exposed to cyclic air oxidation at 900 °C.

3.2.3. Effect of the chemical composition and the chemical segregation at the oxide/metal interface

The chemical segregation, particularly of sulfur, at the interface between metal and oxide scale is known as one of the main causes of spallation of the oxide scales [26, 27]. In our case, the oxide scale spallation mainly occurred at the metal/oxide interface as shown with an example in **Figure 6**. This result was found for the three alloys. Moreover, all samples present internal and intergranular oxidation. As discussed in a previous paper [24], the mass gain corresponding to this internal/intergranular oxidation is small compared to one corresponding to the external oxide scale. This preferential intergranular oxidation was found thicker and

sometimes deeper on the AM alloys compared to the wrought one. This difference was mainly attributed to alloy grain sizes, in which case a grain could act as element reservoir [24].

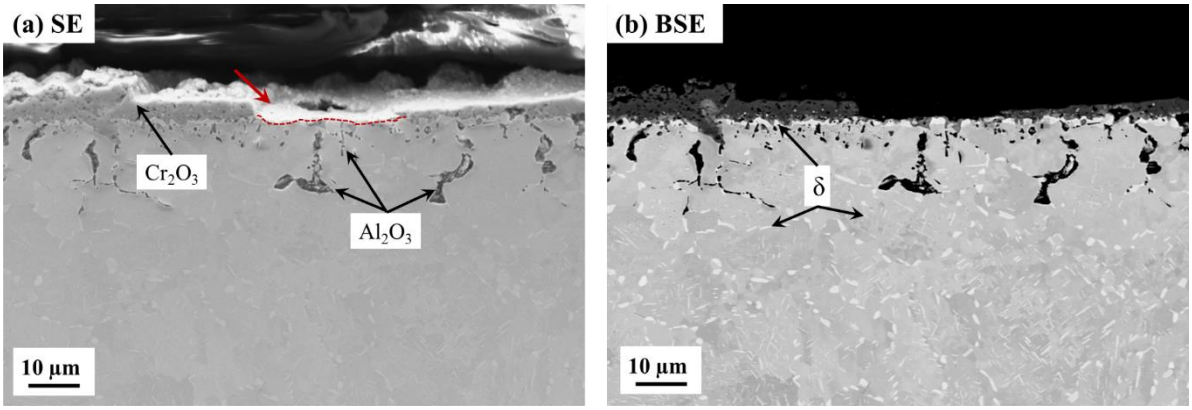

Figure 6. SEM micrographs of the oxide scale spallation occurring at the metal/oxide interface of the alloy 718 produced by LBM (as-built and ground) after 500 air oxidation cycles at 900 °C. Similar results were found on EBM and wrought alloys.

The concentration of minor elements in the alloys of the present study was therefore measured. Results presented in **Figure 7** show that the initial Al and Ti content is too high to quantify these elements accurately by GDMS analysis. However, the analyses were still carried out and the values were found to be in good agreement with the WDS analyses in **Table 3**. The wrought sample has more Co than the AM samples but this low content does not explain the differences in oxidation resistance. The EBM sample shows 0.21 wt.% of Si compared to 0.04 and 0.08 wt.% for the LBM and wrought samples. According to the work of Douglass and Armijo on a Ni-20Cr alloy, 3 wt.% Si is required to form a SiO_2 layer that can act as a diffusion barrier to Cr [28]. However, these authors also found that by forming SiO_2 particles at the metal/oxide interface, the oxide layer could easily spall as found by Romedenne *et al.* on the AM-Hastelloy X alloys [11] . But in this last work, the role of sulfur has not been discussed, the AM alloys presented 20 to 24 ppm wt. of sulfur against 0.6 wt.ppm of S in the wrought alloy. In our case, although the LBM sample presents the lowest content of Si, it presents the worst cyclic oxidation resistance. Moreover, the EBM sample presents the highest content of Si and presents an intermediate oxidation resistance. Therefore, the Si content alone does not explain the results. The elements Y, La and Ce are reactive elements, they are beneficial to the cyclic oxidation behaviour of chromia former alloys, but they must be present in larger quantities, typically 0.1-0.5% [29, 30]. The Re could have a beneficial effect like Pt [31], but it would certainly need several percent. Here, the concentration in Re is likely too low to explain the differences in cyclic oxidation kinetics.

Boron and phosphorus are known to segregate at grain boundaries of alloy 718. A content of 110 wt.ppm of B and 220 wt.ppm of P, improves its creep resistance [32]. The higher content of phosphorus (95 wt.ppm) in the wrought alloy may explain its better resistance to intergranular oxidation as proposed previously [24]. Indeed, for a content between 8 wt.ppm and 130 wt.ppm, phosphorus could inhibit the diffusion of oxygen atoms into grain boundaries of the wrought alloy and would limit the growth of oxides along them [33]. The GDMS analyses results show that the alloys 718 produced by AM have 23 to 36 wt.ppm of S compared to only 0.85 wt.ppm for the wrought alloy. Sulfur in solid solution in the γ-matrix can segregate strongly at the metal/oxide interface with very low concentrations in the bulk. Much less than 1 wt.ppm of sulfur in a millimetre thick sample can affect oxide spallation for an alumina-forming superalloy [26]. The AM samples present 30 times higher contents of sulfur compared to the wrought alloy. This may be the main cause of the fast spallation of their oxide scale. In addition, Mn is known to trap sulfur in the matrix by forming MnS [34]. The high Mn contents of the wrought sample and the EBM sample could explain the better cyclic oxidation resistance at 900 °C of these two alloys compared to the LBM alloy. Similar hypothesis of the interplay between sulfur and manganese for a chromia forming alloy was tested previously with stainless steel 304 [35].

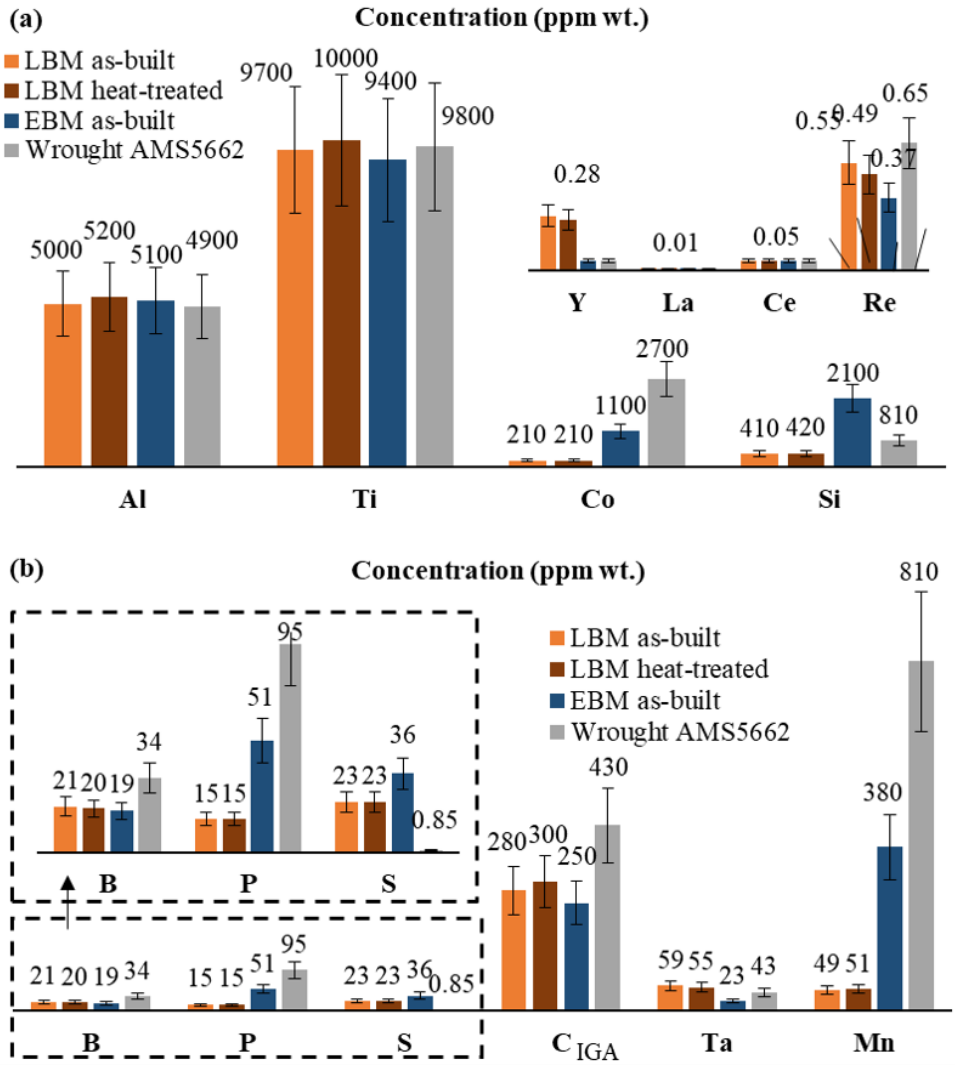

Figure 7. GDMS analyses of minor elements and IGA analyses of the carbon element present in the various alloys 718.

Table 3. Chemical compositions of the different 718 alloys (EPMA and GDMS) used as input data for Thermocalc^{TM} calculations.

718 alloys		EPMA-WDS (%)							IGA (ppm)	GDMS (ppm)	
		Ni	Cr	Fe	Al	Ti	Nb	Mo	C	Mn	S
LBM	wt.	bal.	20.1	19.2	0.4	1.0	5.0	2.9	280	51	23
	at.	bal.	22.3	19.9	0.9	1.2	3.1	1.7	1341	53	41
EBM	wt.	bal.	21.3	19.4	0.5	1.1	5.0	2.9	250	380	36
	at.	bal.	23.1	19.6	1.1	1.3	3.0	1.7	1175	391	63
Wrought	wt.	bal.	20.4	18.3	0.4	0.9	4.0	2.7	430	810	0.85
	at.	bal.	22.9	19.1	0.9	1.1	2.5	1.6	2078	860	1.55

3.2.4. Determination of the quantity of sulfur at the metal/oxide interface

Sulfur can segregate at the metal/oxide interface and affect the adhesion of the oxide layer, for both alumina former alloys [36] and chromia former alloys [37, 38]. This result is very well known for alumina-forming alloys [36-39]. With these alloys, even lower amounts of sulfur (between 0.1 and 1 wt ppm) were shown to affect the spallation behaviour. The segregated sulfur is in equilibrium with the sulfur in solution in the γ-Ni phase. This sulfur in solution in the γ-Ni phase is called here the "free" sulfur, to differentiate it from the sulfur "trapped" in sulfides. The quantity of free sulfur in the 718 alloys oxidised at 900°C was determined using thermodynamic calculations. In earlier works, Meier, Pettit and Smialek used the concept of the solubility product to discuss the effect of Hf and Y on the trapping of sulfur [27]. In the present work, this approach was extended with calculations considering the global concentrations of the main alloying elements (Ni-Cr-Fe-Al-Ti-Nb-Mo), which were quantified by microprobe analyses, as well as the global concentrations of S and Mn, which were quantified by GDMS, **Table 3**. These calculations were carried out using the Thermocalc^{TM} software, with the Thermo-Calc NI28 Ni-based alloys database (accessed on February, 14th 2020) which is under development and now includes S. The results are presented in **Table 4**.

First, the calculation of the equilibrium phases at 900 °C allows to determine the most stable sulfides as well as the amount of S remaining in solution in γ-Ni. From these results, the quantity of S trapped in the sulphides was determined in each alloy.

Subsequently, equilibrium segregation calculations were performed based on the amount of free sulfur in solution in the γ-Ni phase. For this calculation, the segregation of S at grain boundaries was not considered, assuming that the grain boundaries behave like the surface. Furthermore, the enthalpy of S segregation was considered the same in the γ-phase of the alloy 718 and in pure Ni. Moreover, the hypothesis that S segregates at the metal/oxide interface as it segregates at a free surface was made. Therefore, the calculated segregation values are certainly overestimated, but these calculations allow comparison of the three alloys.

The phenomenon of equilibrium segregation can be approximated to chemisorption with a lowering of the surface energy. It can therefore be calculated with the Langmuir-McLean relationship for a binary system. The surface coverage level Θ corresponding to the segregation of S at the surface is defined as the concentration of S at the surface divided by the maximum concentration at saturation of the surface atomic layer. It is assumed here that 50% of the surface sites are occupied by the S at saturation (Θ = 1) [40]. The surface coverage level is determined from the Langmuir-McLean adsorption parameter (β_p) presented in **Equations (1)** and **(2)**, with X_S^{γ} the concentration of free S in the nickel volume and $\Delta G'$ the free enthalpy of sulfur segregation (-135 kJ.mol-1) [40].

$$\text{———} \exp\left(\text{——}\right) \text{——} \qquad \textbf{(1)}$$

$$\text{———} \qquad \textbf{(2)}$$

From **Equations (1)** and **(2)**, the surface coverage level Θ was determined based on the atomic fraction of S in solution in γ-Ni. These calculations allow determination of the minimum sulfur concentration at which S starts to segregate significantly at the surface. Results presented in **Figure 8**, show that about 0.01 at.ppm of S in solution in γ-Ni is sufficient to have a significant amount (1%) of S on the surface, and to have a possible consequence on the adhesion of the oxide layer. The AM alloys contain much more S, only a very small proportion of the S in alloy 718 needs to be in solution in the gamma phase in order to have a significant segregation and to generate oxide spallation. In our case, the AM

alloys have around 30 wt.ppm of sulfur which is considerably high enough to find sulfur at the oxide/metal interface.

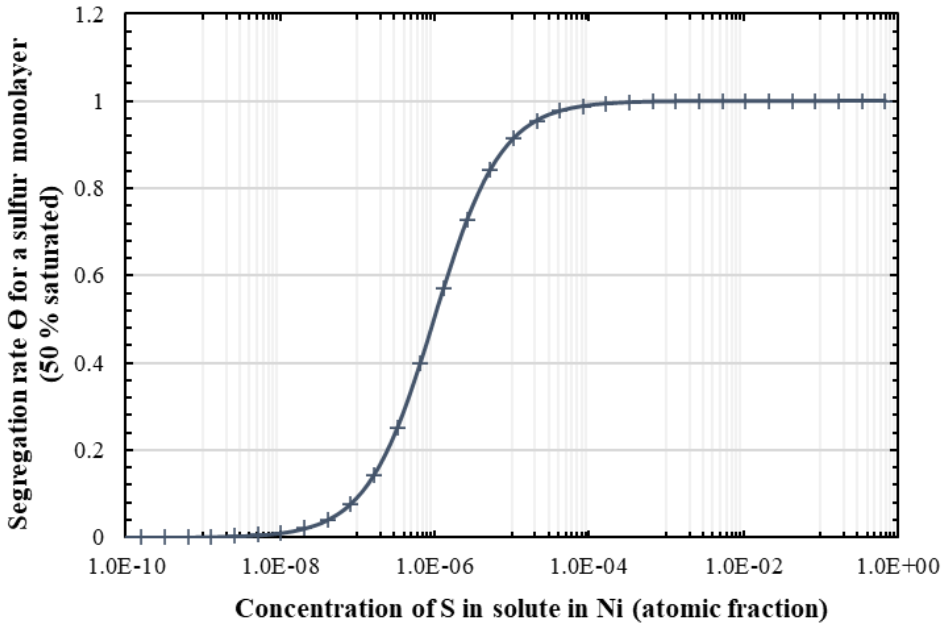

Figure 8. Sulfur surface coverage level on the first atomic layer of a nickel surface as a function of the concentration of free S in the volume, calculations conducted at 900 °C.

Thermodynamic calculations (using Thermocalc^{TM} software) were carried out considering all the sulfides described in the Thermo-Calc NI28 Ni-based alloys database (accessed on February, 14th 2020) and set as **Condition 1** in **Table 4**. The Alabandite (Cr,Fe,Mn)S (NaCl, cF8, Fm3m) and Pyrrhotite (Al,Co,Cr,Fe,Mn,Nb,Ti)S type sulfides were considered. However, calculation results showed that only Pyrrhotite type sulfides are expected to be present. Under these conditions, the amount of S in the γ-Ni phase of the three alloys reaches values between 0.072 and 0.12 at.ppm. These values are sufficiently high for S to segregate at the surface with a surface coverage level around 10% for LBM and wrought alloys, compared to 6.8% for the EBM alloy. However, if we assume that sulfur is responsible for the catastrophic spalling observed during thermal cycling, these results do not correspond to the mass variation kinetics shown in **Figure 1**. Indeed, the wrought sample should present less free sulfur in γ-Ni, and therefore the lowest quantity of segregated S at the metal/oxide interface, which is not the case.

Consequently, new calculations were performed, considering only Alabandite (Cr,Fe,Mn)S (NaCl, cF8, Fm3m) sulfides (**Condition 2**, from **Table 4**). Under these conditions, results show quantities of free S in γ-Ni consistent with the kinetic oxidation results. Indeed, the LBM sample spalled faster than the two other samples, and according to the thermodynamic calculations, it is also the one with the highest S segregation (Θ = 54%). The wrought sample, which spalled much slower than the other two alloys, has the lowest S segregation rate (Θ = 28%). The EBM sample, which exhibits intermediate oxidation kinetic, has intermediate segregation rate (Θ = 31%).

In order to validate our hypothesis that S segregation occurs from S in solution in the γ-Ni phase, without affecting the volume fractions in sulfides, the amount of S segregated at the surface was evaluated and compared to the amount of S present in the γ-Ni phase. Assuming a sample thickness of 1 mm and a 50% coverage rate of an S layer of half Ni unit cell parameter, set as 0.352/2 nm thickness. The proportion of S that segregates was found very low (**Table 4**). Thus, the segregation of S does not lead to the depletion of the S concentration in γ-Ni, and thus does not lead to the dissolution of sulfur-trapping precipitates.

To summarize, 77 to 99.9% of the sulfur present in the alloy is trapped in the sulfides. The remaining quantities are in solution in γ and a very small proportion (≈ 0.02 to 0.05%) is segregated at the metal/oxide interface.

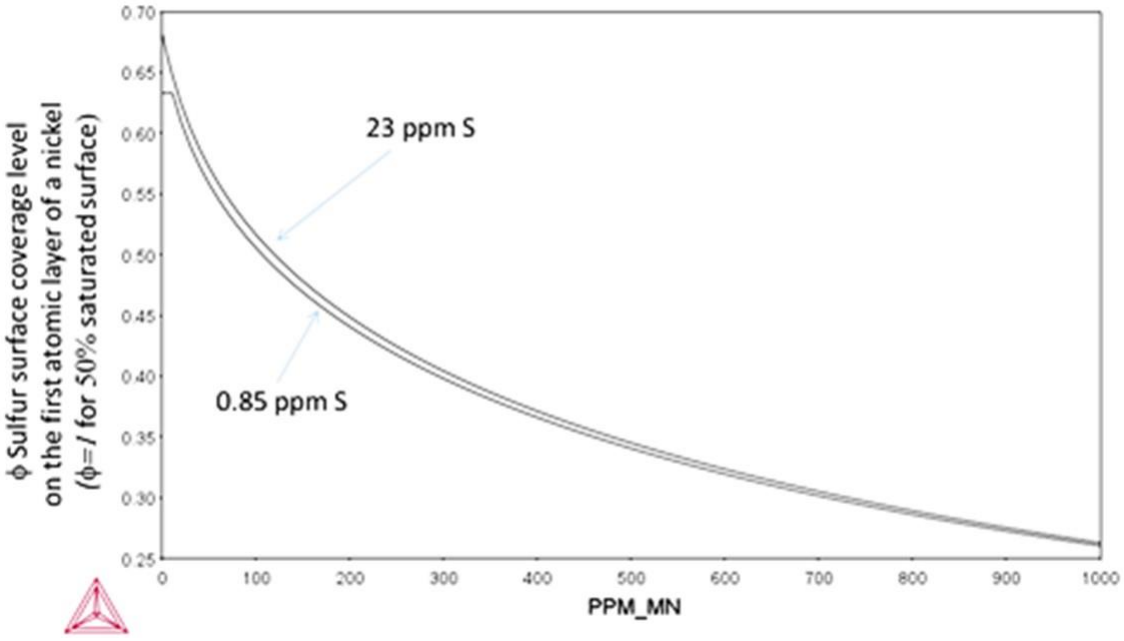

Figure 9. Sulfur coverage level at the surface of the gamma phase of alloy 718 as a function of the concentration of Mn in the alloy. Calculations conducted at 900 °C (Condition 2, see text).

Conditions 2 : γ (FCC_L12#1) ; δ (Ni3TA_D0A) ; **(Cr,Fe,Mn)S (ALABANDITE)**	**LBM**	γ (FCC_L12#1): 8.74×10^{-1} δ (Ni3TA_D0A): 1.26×10^{-1} ALABANDITE: 1.25×10^{-4}	4.16×10^{-5}	1.16×10^{-6}	97.5	5.4×10^{-1}	0.011

In **Table 4**, it is noticeable that the concentration of sulfur in solution in the γ-phase is similar for the three alloys, despite the fact that the total concentration of sulfur is much higher (> 20 wt.ppm) for the LBM and EBM samples than for the wrought alloy (< 1 wt.ppm). As the Mn concentration is much higher than the S concentration, the solubility product (K_S= [Mn].[S]) sets the value of [S] at in solution at equilibrium for a given initial concentration of Mn. This effect is illustrated in **Figure 9** which presents the S coverage level at the surface of the γ-phase of alloy 718, as a function of the total concentration of Mn in the alloy. On this figure, it can be seen that the S segregation which is a direct function of the concentration of S in solution in γ-phase decreases with increasing levels of Mn. It can be seen also that the S segregation level is similar for two very different total concentrations of S in the alloys. These calculations show that Mn controls the level of S segregation at the surface of the gamma phase.

The results of calculations under **Condition 2** (alabandite only), show a significant segregation of S at the surface (28 to 54% of an atomic half-monolayer). For comparison, Hou and Moskito measured S contents at the metal/oxide interface of 4 at% or close to half to a monolayer in a Fe-40Al alumina-forming alloy containing 20 wt.ppm of sulfur impurity in its bulk [39]. Here, the determined S segregations are certainly sufficient to embrittle the metal/oxide interface and cause premature spallation of the 718 LBM samples. Calculations performed considering only Alabandite-type sulfides are consistent with the oxidation kinetics in **Figure 1**, nevertheless the reality could be more complicated as discussed below.

Table 4. Determination of phase volume fractions and the quantity of sulfur in γ-Ni using Thermo-Calc NI28 Ni-based alloys database (accessed on February, 14th 2020), calculation were conducted at 900°C, and determination of the resulting equilibrium segregation at the surface.

Considered phases (Thermocalc™)	**Conditions 1 :** γ (FCC_L12#1) ; δ (Ni3TA_D0A) ; **(Al,Co,Cr,Fe,Mn,Nb,Ti)S (PYRRHOTITE)** **(Cr,Fe,Mn)S (ALABANDITE)**					
Samples	**Wrought**	**EBM**	**LBM**		**Wrought**	**EBM**
Obtained phases (fraction vol.) (Thermocalc™)	γ (FCC_L12#1): 9.11×10^{-1} δ (Ni3TA_D0A): 8.92×10^{-2} PYRRHOTITE: 3.95×10^{-6}	γ (FCC_L12#1): 8.67×10^{-1} δ (Ni3TA_D0A): 1.33×10^{-1} PYRRHOTITE: 1.73×10^{-4}	γ (FCC_L12#1): 8.73×10^{-1} δ (Ni3TA_D0A): 1.27×10^{-1} PYRRHOTITE: 1.11×10^{-4}		γ (FCC_L12#1): 9.11×10^{-1} δ (Ni3TA_D0A): 8.92×10^{-2} ALABANDITE: 4.65×10^{-6}	γ (FCC_L12#1): 8.67×10^{-1} δ (Ni3TA_D0A): 1.33×10^{-1} ALABANDITE: 1.96×10^{-4}
Total amount of S (GDMS) (at. fraction)	1.53×10^{-6}	6.51×10^{-5}	4.16×10^{-5}		1.53×10^{-6}	6.51×10^{-5}
S in γ (at. fraction) (Thermocalc™)	1.17×10^{-7}	7.23×10^{-8}	1.09×10^{-7}		3.81×10^{-7}	4.39×10^{-7}
Percentage of S trapped in sulphides	93.0	99.9	99.8		77.2	99.4
Segregation rate Θ eq. (2)	1.1×10^{-1}	6.9×10^{-2}	1.0×10^{-1}		2.8×10^{-1}	3.1×10^{-1}
Percentage of S segregated at the surface	0.021	0.022	0.022		0.018	0.017

According to Sun *et al.*, cast 718 alloy may exhibit sulfides rich in Nb, Ti and Ni [41]. However, these sulfides are nanometric, they are difficult to observe and their crystallographic structures have not been identified. According to the literature, the alloy 718 can also present carbosulfides like $(Ti,Nb)_2CS$ type which have the same crystallographic nature as the Pyrrhotite (P63/mmc) type sulphides [42, 43]. Thus, additional calculations taking into account the carbon content would be necessary to go further. It is also possible that the database for sulfides is not accurate enough or for a nucleation reason, Alabandite type sulfides are present and not Pyrrhotite type sulfides. Smaller scale chemical and microstructural characterizations using transmission electronic microscopy are required to identify the precise nature of sulfides or carbosulfides in the γ matrix of 718 alloys. Moreover, it is also possible to verify experimentally whether S is responsible for these catastrophic spalling differences, by performing cyclic oxidation tests on the three alloys after desulphurization under H_2 or by polishing them repeatedly after a few cycles at high temperature [44]. In the present paper, results showed that the idea that sulfur segregation could be responsible for catastrophic spallation could be applied to a commercial chromia forming alloy, since thermodynamic calculations showed that the amount of sulfur measured in our alloy is sufficient to segregate in large concentrations at the metal/oxide interface despite the formation of sulphides in the bulk.

Conclusions

Previous results regarding the air isothermal oxidation resistance at 850 °C of several 718 alloys, showed that the wrought alloy was only slightly more resistant to oxidation in terms of mass gain and intergranular oxidation compared to the ones produced by LBM and EBM [1] [24]. However, in the present paper, the cyclic air oxidation tests carried out at 900 °C on the same alloys from the same batches, showed large differences in terms of the rate of oxide layer spallation. This is an important result that may limit the use of 718 alloys produced by AM process. The grinding and the heat-treatment delay the catastrophic spallation of the LBM sample by about 100 cycles. The oxide scale of LBM samples spalled much faster than the one found on EBM and wrought samples. The hypothesis that these differences in oxide layer adhesion could be attributed to the sulfur and manganese content in the alloys was discussed in details in this paper. The LBM and EBM samples show sulfur content between 20 and 40 wt.ppm compared to only 0.9 wt.ppm for the wrought sample. In addition, the wrought and the EBM samples have more Mn, respectively 380 and 810 wt.ppm, compared to 50 wt.ppm. in the LBM sample. This element, capable of trapping S in the matrix, as shown

by the thermodynamic calculations using a new Calphad-type database, would limit the segregation of the latter at the metal/oxide interface. However, the presence of these sulfides and possibly the presence of carbosulfides, both remain to be confirmed by high resolution microscopies and nano-scale chemical analyses.

Acknowledgements

The authors thank Arnaud Proietti and Sophie Gouy, both from the Raimond Castaing Microanalysis Centre (Toulouse, France). We thank them for their analyses and constructive discussions for the EBSD results and EPMA-WDS results. We also thank Boris Albouy and Jérémy Berot-Lartigue, from Eurofins EAG (Toulouse, France), for their IGA and GDMS analysis.

References

[1] T. Sanviemvongsak, D. Monceau, B. Macquaire, High temperature oxidation of IN 718 manufactured by laser beam melting and electron beam melting: Effect of surface topography, Corrosion Science 141 (2018) 127-145.
[2] C. Juillet, A. Oudriss, J. Balmain, X. Feaugas, F. Pedraza, Characterization and oxidation resistance of additive manufactured and forged IN718 Ni-based superalloys, Corrosion Science (2018).
[3] H. Yu, S. Hayashi, K. Kakehi, Y.-L. Kuo, Study of Formed Oxides in IN718 Alloy during the Fabrication by Selective Laser Melting and Electron Beam Melting, Metals 9(1) (2018).
[4] Q. Jia, D. Gu, Selective laser melting additive manufacturing of Inconel 718 superalloy parts: Densification, microstructure and properties, Journal of Alloys and Compounds 585 (2014) 713-721.
[5] Y.-J. Kang, S. Yang, Y.-K. Kim, B. AlMangour, K.-A. Lee, Effect of post-treatment on the microstructure and high-temperature oxidation behaviour of additively manufactured inconel 718 alloy, Corrosion Science 158 (2019) 108082.
[6] M. Calandri, D. Manfredi, F. Calignano, E.P. Ambrosio, S. Biamino, R. Lupoi, D. Ugues, Solution Treatment Study of Inconel 718 Produced by SLM Additive Technique in View of the Oxidation Resistance, Advanced Engineering Materials 20(11) (2018) 1800351.
[7] E. Sadeghi, P. Karimi, S. Momeni, M. Seifi, A. Eklund, J. Andersson, Influence of thermal post treatments on microstructure and oxidation behavior of EB-PBF manufactured Alloy 718, Materials Characterization 150 (2019) 236-251.
[8] J.K. Tien, J.M. Davidson, Oxide spallation mechanisms, in: J.V. Cathcart (Ed.) Stress Effects and the Oxidation of Metals Proc. TMS-AIME Fall Meeting, TMS-AIME, New York (1975), 1975, p. 200.
[9] H.E. Evans, A. Strawbridge, R.A. Carolan, C.B. Ponton, Creep effects on the spallation of an alumina layer from a NiCrAlY coating, Materials Science and Engineering A225 (1997) 1-8.
[10] K.A. Unocic, L.M. Kolbus, R.R. Dehoff, S.N. Dryepondt, B.A. Pint, High-Temperature Performance of UNS N07718 Processed by Additive Manufacturing, Corrosion 2014 (4478) (2014).
[11] M. Romedenne, R. Pillai, M. Kirka, S. Dryepondt, High temperature air oxidation behavior of Hastelloy X processed by Electron Beam Melting (EBM) and Selective Laser Melting (SLM), Corrosion Science 171 (2020) 108647.

[12] A. Casadebaigt, J. Hugues, D. Monceau, Influence of Microstructure and Surface Roughness on Oxidation Kinetics at 500–600 °C of Ti–6Al–4V Alloy Fabricated by Additive Manufacturing, Oxidation of Metals 90(5) (2018) 633-648.
[13] N. Ramenatte, A. Vernouillet, S. Mathieu, A. Vande Put, M. Vilasi, D. Monceau, A comparison of the high-temperature oxidation behaviour of conventional wrought and laser beam melted Inconel 625, Corrosion Science 164 (2020) 108347.
[14] T. Sanviemvongsak, Oxydation et corrosion à haute température de superalliages à base de nickel issus de la fabrication additive, University of Toulouse, 2020.
[15] D. Monceau, Monte-Carlo simulation code of cyclic oxidation kinetics, Private com. (1998).
[16] S. Sureau, D. Poquillon, D. Monceau, Numerical simulation of cyclic oxidation kinetics with automatic fitting of experimental data, Scripta Materialia, 2007, pp. 233-236.
[17] D. Monceau, C. Desgranges, Python code for Monte Carlo simulation of Cyclic Oxidation Kinetics, private communication (2020).
[18] C.E. Lowell, C.A. Barrett, R.W. Palmer, J.V. Auping, H.B. Probst, COSP: a computer model of cyclic oxidation, Oxidation of Metals 36(1/2) (1991) 81-112.
[19] D. Poquillon, D. Monceau, Prediction of high temperature cyclic oxidation kinetics with simple statistical spalling model, in: L. P.K, B. R.A., K. D.L., W. R.P., H. D.G., T. P.F. (Eds.) TMS Annual Meeting, TMS, San Diego, 2003, pp. 165-172.
[20] J.L. Smialek, Universal characteristics of an interfacial spalling cyclic oxidation model, Acta Materialia 52(8) (2004) 2111-2121.
[21] K.A. Al-hatab, M.A. Al-bukhaiti, U. Krupp, M. Kantehm, Cyclic Oxidation Behavior of IN 718 Superalloy in Air at High Temperatures, Oxidation of Metals 75(3) (2011) 209-228.
[22] D. Zhang, W. Niu, X. Cao, Z. Liu, Effect of standard heat treatment on the microstructure and mechanical properties of selective laser melting manufactured Inconel 718 superalloy, Materials Science and Engineering: A 644(Supplement C) (2015) 32-40.
[23] C.S. McDowell, S.N. Basu, Alloy-grain-size dependence of the effectiveness of silica coatings as oxidation barriers on stainless steel, Oxidation of Metals 43(3) (1995) 263-277.
[24] T. Sanviemvongsak, D. Monceau, C. Desgranges, B. Macquaire, Intergranular oxidation of Ni-base alloy 718 with a focus on additive manufacturing, Corrosion Science 170 (2020) 108684.
[25] A.G. Evans, M.Y. He, J.W. Hutchinson, Effect of interface undulations on the thermal fatigue of thin films and scales on metal substrates, Acta Materialia 45(9) (1997) 3543-3554.
[26] J.L. Smialek, Effect of sulfur removal on Al2O3 scale adhesion, Metallurgical and materials transactions A 22A (1991) 739-752.
[27] G.H. Meier, F.S. Pettit, J.L. Smialek, The effects of reactive element additions and sulfur removal on the adherence of alumina to Ni- and Fe-base alloys, Materials and Corrosion 46 (1995) 232-240.
[28] D.L. Douglass, J.S. Armijo, The effect of silicon and manganese on the oxidation mechanism of Ni-20 Cr, Oxidation of Metals 2(2) (1970) 207-231.
[29] B. Pieraggi, R.A. Rapp, Chromia Scale Growth in Alloy Oxidation and the Reactive Element Effect, Journal of the Electrochemical Society 140(10) (1993) 2844-2850.
[30] S. Chevalier, G. Bonnet, G. Borchardt, J.C. Colson, J.P. Larpin, Mechanisms involved by reactive elements upon high temperature chromia scale growth, High Temperature Corrosion and Protection of Materials 5, Pts 1 and 2 369-3 (2001) 327-336.
[31] J.K. Tien, F.S. Pettit, Mechanism of oxide adherence on Fe-25Cr-4Al (Y or Sc) Alloy, Metallurgical Transactions 3 (1972) 1587.
[32] M.K. Miller, J.A. Horton, W.D. Cao, R.L. Kennedy, Characterization of the Effects of Boron and Phosphorus Additions to the Nickel-Based Superalloy 718, J. Phys. IV France 06(C5) (1996) C5-241-C5-246.
[33] W.R. Sun, S.R. Guo, J.H. Lee, N.K. Park, Y.S. Yoo, S.J. Choe, Z.Q. Hu, Effects of phosphorus on the δ-Ni3Nb phase precipitation and the stress rupture properties in alloy 718, Materials Science and Engineering: A 247(1) (1998) 173-179.
[34] J.L. Robinson, M.H. Scott, Liquation cracking during the welding of austenitic stainless steels and nickel alloys, Philosophical Transactions of the Royal Society of London. Series A, Mathematical and Physical Sciences 295(1413) (1980) 105-117.

[35] C. Pascal, V. Parry, E. Fedorova, M. Braccini, P. Chemelle, N. Meyer, D. Oquab, D. Monceau, Y. Wouters, M. Mantel, Breakaway oxidation of austenitic stainless steels induced by alloyed sulphur, Corrosion Science 93 (2015) 100-108.
[36] J.L. Smialek, The effect of sulfur on Al2O3 scale adhesion, in: T.I.o. Metals (Ed.) Microscopy of oxidation, Cambridge, 1990.
[37] D.G. Lees, On the reasons for the effects of dispersions of stable oxides and additions of reactive elements on the adhesion and growth-mechanisms of chromia and alumina scales-the “sulfur effect”, Oxidation of Metals 27(1-2) (1987) 75-81.
[38] J. Grabke, D. Wiemer, H. Viefhaus, Segregation of sulfur during growth of oxide scales, Applied Surface Science 47 (1991) 243-250.
[39] P.Y. Hou, J. Moskito, Sulfur segregation to Al2O3 interfaces studied by Field Emission-Auger Electron Spectroscopy, Oxidation of metals 59(5/6) (2003) 559-574.
[40] T. Miyahara, K. Stolt, D.A. reed, H.K. Birnbaum, Sulfur segregation on nickel, Scripta Metallurgica et Materialia 19 (1985) 117-121.
[41] M. Sundararaman, P. Mukhopadhyay, S. Banerjee, Carbide precipitation in nickel bas superalloys 718 and 625 and their effect on mechanical properties The Minerals, Metals & Materials Society Superalloys 718,625,706 and Various Derivatives (1997) 367 - 378.
[42] R. Vincent, Precipitation around welds in the nickel-base superalloy, Inconel 718, Acta Metallurgica 33(7) (1985) 1205-1216.
[43] S. Vernier, E. Andrieu, L. Laffont, Flash oxidation tests to evidence the segregation of boron at the grain boundaries of superalloy Inconel 718, Materialia 15 (2021) 100989.
[44] J.L. Smialek, D.T. Jayne, J.C. Schaeffer, W.H. Murphy, Effects of hydrogen annealing, sulfur segregation, and diffusion on the cyclic oxidation resistance of superalloys: a review, Thin Solid Films 253 (1994) 285-292.

CRediT author statement

Tom Sanviemvongsak: Methodology, Investigation, Supervision, Visualization, Writing - Original Draft

Daniel Monceau: Supervision, Validation, Writing - Review & Editing, Project administration

Martin Madelain: Methodology, Investigation

Clara Desgranges: Formal analysis, Writing - Review & Editing

James Smialek: Validation, Writing - Review & Editing

Bruno Macquaire: Resources, Funding acquisition, Writing - Review & Editing

Declaration of interests

☒ The authors declare that they have no known competing financial interests or personal relationships that could have appeared to influence the work reported in this paper.

☐The authors declare the following financial interests/personal relationships which may be considered as potential competing interests:

Highlights

1. AM 718 alloys spall faster than the wrought one under cyclic oxidation condition
2. Oxide spallation is delayed for ground and heat-treated samples
3. AM samples have higher sulfur content than wrought ones
4. Sulfur and manganese contents can explain the differences in spallation rates
5. Thermodynamical calculations quantify the sulfur trapping by manganese